Materials Today Chemistry 55 (2026) 103832

Contents lists available at ScienceDirect

Materials Today Chemistry

journal homepage: www.journals.elsevier.com/materials-today-chemistry/

Mechanical tough double conductive network hydrogel for continuously stabilizing soft bioelectronic interface

Yumeng Zhang [a,b,1], Chang Zhu [a,b,1], Han Ouyang [a,b], Xiangxiang Wang [a,b], Jian Cheng [a,b], Xiong Pu [a,b], Engui Wang [b,*], Zhou Li [c,d,**]

[a] Beijing Institute of Nanoenergy and Nanosystems, Chinese Academy of Sciences, Beijing, 101400, China
[b] School of Nanoscience and Engineering, College of Materials Science and Opto-Electronic, Technology, University of Chinese Academy of Sciences, Beijing, 100049, China
[c] Vita Tech Innovation Center, Beijing Tsinghua Changgung Hospital, School of Clinical Medicine, Tsinghua University, Beijing, 100084, China
[d] School of Biomedical Engineering, Tsinghua University, Beijing, 100084, China

ARTICLE INFO

Keywords:
Conductive hydrogel
Bioelectronic interface
MXene

ABSTRACT

Soft bioelectronic interfaces can be utilized in brain-computer interfaces, neuromodulation, and cardiac pacing, emerging as a rising technology. However, the development of adapted bioelectronic interface materials remains challenging, due to ongoing issues with the adaptation of moduli and the balance of signal transmission between bioelectronic interfaces and biological interfaces. Inspired by the design of a multi-network structure, a hydrogel with ion electron double conductive network was developed, which further simplifies the preparation process while ensuring the conductivity, strength, and toughness, and forms a network structure of MXene and PEDOT: PSS in a PVA matrix. The obtained hydrogel shows the comprehensive properties supporting this synergy: good conductivity (0.913 mS cm^{-1}), wide strain response range (0-500%), high Young's modulus (74 kPa), high signal fidelity, and excellent stability (10 days). The core progress lies in simplifying the preparation process and components, ensuring that the material adapts to the skin modulus while utilizing an ion-electron dual conductive network as the epidermal electrode, which can accurately collect electrocardiogram and electromyography signals. This study provides a scalable and low-cost material paradigm for soft bioelectronic interfaces.

1. Introduction

Bioelectronics by establishing bidirectional channels of charge and information, facilitates the real-time reading, decoding, and precise feedback of electrophysiological activities in cells, tissues, and organs outside the body, laying the groundwork for precision medicine and personalized treatment [1–4]. However, the elastic modulus of soft tissues such as human skin, brain, or heart muscle differs by 3 to 6 orders of magnitude from that of traditional silicon-based metal electrodes [5–8]. This leads to micro-motion shear of the implanted device during breathing, heartbeat, or joint flexion and extension, inducing inflammatory cascade reactions, fiber capsule embedding, and interface impedance drift, thereby resulting in signal attenuation, elevated stimulation threshold, and tissue damage [9–11]. Meanwhile, a significant charge transfer potential barrier exists at the solid-liquid interface between ionic biological signals and electronic devices, further limiting high-fidelity recording and efficient excitation [12]. To overcome the above challenges, researchers systematically explored soft conductive materials, such as two-dimensional materials (graphene), conductive polymers (polypyrrole), and bioabsorbable metals (Mg, Zn, Mo) [13]. Although two-dimensional materials have excellent in-plane electrical conductivity, their out-of-plane brittleness and tear toughness are relatively low [14]. Conductive polymers can achieve dual conduction of ions and electrons. However, their tensile strength is usually less than 10 MPa, and when exposed to salt-containing fluids for a long time, they are prone to debonding and reduced electrical conductivity [15].

* Corresponding author. School of Nanoscience and Engineering, School of Chemical Sciences, University of Chinese Academy of Sciences, Beijing 100049, China.
** Corresponding author. Vita Tech Innovation Center, Beijing Tsinghua Changgung Hospital, School of Clinical Medicine, Tsinghua University, Beijing, 100084, China.
E-mail addresses: wangengui@ucas.ac.cn (E. Wang), li_zhou@tsinghua.edu.cn (Z. Li).
[1] These authors contributed equally to this work.

https://doi.org/10.1016/j.mtchem.2026.103832
Received 17 February 2026; Received in revised form 2 June 2026; Accepted 29 June 2026

Bioabsorbable metals have the ability to provide temporary scaffolds and high charge injection, but there is an inherent contradiction between the corrosion rate and mechanical strength [16]. In contrast, hydrogel composites have a modulus similar to that of skin and can also be modified to achieve ultimate capability [17,18]. It has evolved from a conductive filler carrier to a mainstream platform for bioelectronic interfaces, and continues to develop towards enhanced degradability, stretchability, and closed-loop intelligence [19–21].

Although traditional hydrogels possess bionic modulus and controllable networks, they are intrinsically insulating, have poor toughness, and are prone to swelling and fatigue [22,23]. Therefore, researchers often modify traditional hydrogels [24–26]. In recent years, researchers have oxidized and polymerized aniline monomers within the hydrogel network to form interpenetrating hydrogel methacrylate–polyaniline hydrogels [27]. The conductive polyaniline segments provide ion-electron dual channels. The hydrogel skeleton maintains a high-water content and cell affinity. Meanwhile, the dual network energy dissipation mechanism increases the breaking energy by an order of magnitude. After soaking in PBS for 30 days, it still maintains an electrical conductivity of over 90%, providing a new model for stretchable and degradable bioelectronic interfaces [27]. To address the aforementioned difficulties in bioelectronic interfaces, the hydrogel composite system is required to have an appropriate mechanical modulus, high signal transmission capacity, and long-term stability. Hydrogel composites can significantly reduce interfacial shear stress by introducing conductive nanophases or conjugated polymers into a three-dimensional hydrophilic network, thereby achieving an elastic modulus of the same order of magnitude as that of soft tissues [28]. More importantly, the high water content and porous structure of hydrogels provide continuous channels for ion migration [29]. By adjusting the interlayer spacing of the nanosheets [30], the doping degree of the electrolyte [31], or the interface capacitance [32], the interface impedance can be reduced, the charge injection capacity can be enhanced, and the dual requirements of microvolt-level neural signal

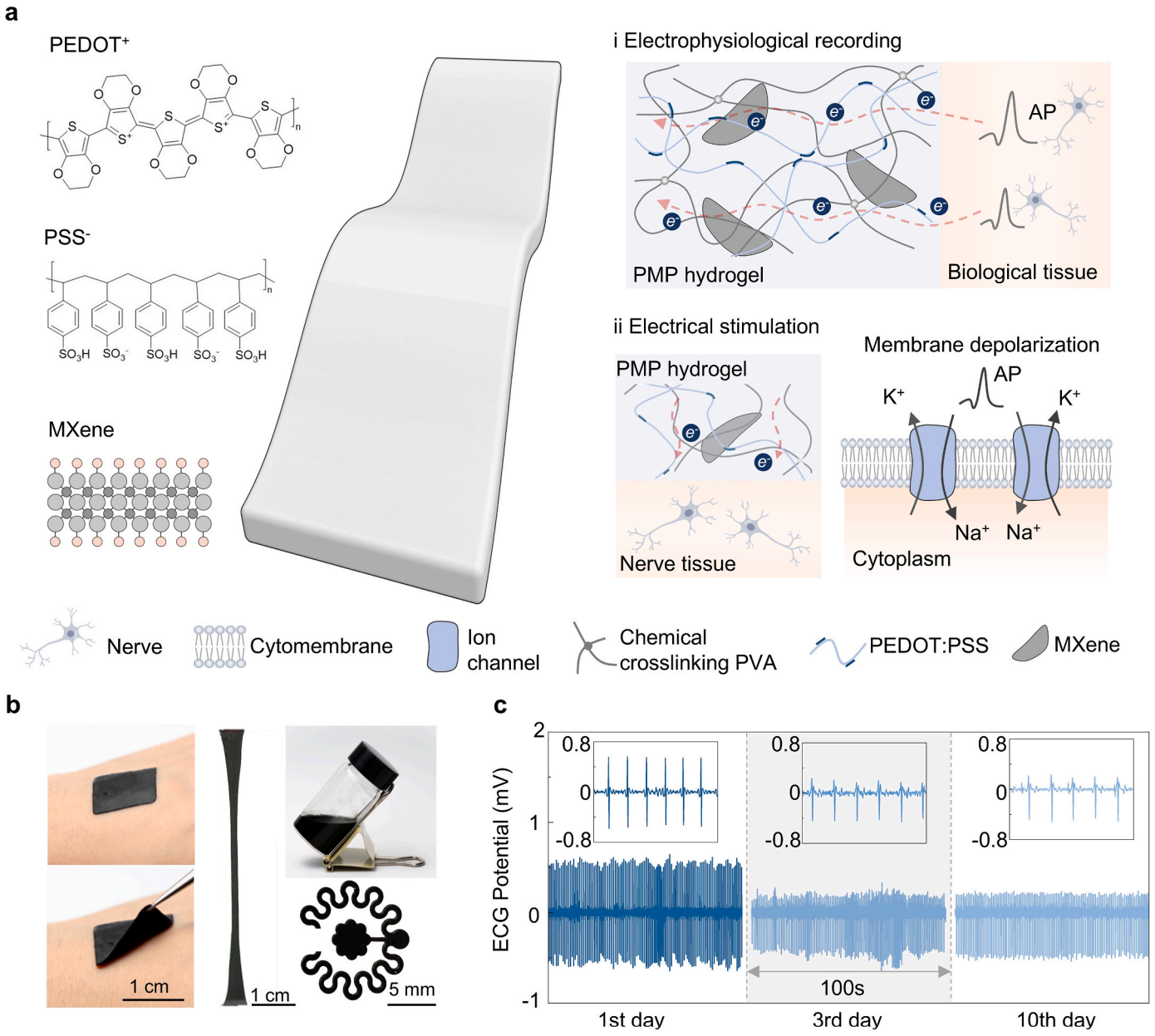

Fig. 1. Structure, performance and physical display of PMP hydrogel. **a**. Schematic diagram of PMP hydrogel network structure and its application. **b**. PMP hydrogel electrode. **c**. PMP hydrogel ECG test results.

recording and milliampere-level safe stimulation can be met. Common modification methods include designing multi-network structures [33], in-situ composite of conductive components [34], and physical structural design [35], etc. However, in the actual modification process, conductivity and mechanical properties often have a trade-off, and precise control of network structure and long-term stability are difficult to achieve simultaneously, becoming the core bottleneck restricting performance breakthroughs [36]. The preparation of hydrogel composite systems suitable for bioelectronic interfaces remains a challenge [37].

This study reports a solid PVA MXene PEDOT: PSS (PMP) hydrogel, which forms an ion electron double conductivity enhancement network to achieve a balanced combination of conductivity, ductility and biocompatibility (Fig. 1a and b). MXene electrically reinforces the PEDOT:PSS network through electrostatic interactions while forming continuous conductive pathways, and PVA serves as the structural framework via surface hydrogen bonding. After freeze-thaw cycles, the hydrogel achieves flexibility, adhesion, long-term stability, and high-fidelity signal transmission, enabling human ECG/EMG monitoring (Fig. 1c) and simultaneous neural stimulation and recording in rats.

2. Results and discussion

2.1. Microstructure and mechanical properties of PMP hydrogel

The synthesis process of the ion-electron dual-conductive reinforced network toughening hydrogel developed in this study (for details, see the experimental section). It can be observed from Fig. 2e that the prepared MXene has a clear and uniform sheet-like structure, while Ti is evenly distributed, confirming its good electrical conductivity. To simplify the preparation process of PMP hydrogel, we will prepare the pre-prepared PVA solution, MXene solution, and PEDOT: PSS solution in different proportions to form the precursor. After stirring evenly at room temperature, the PMP hydrogel precursor was placed under high-

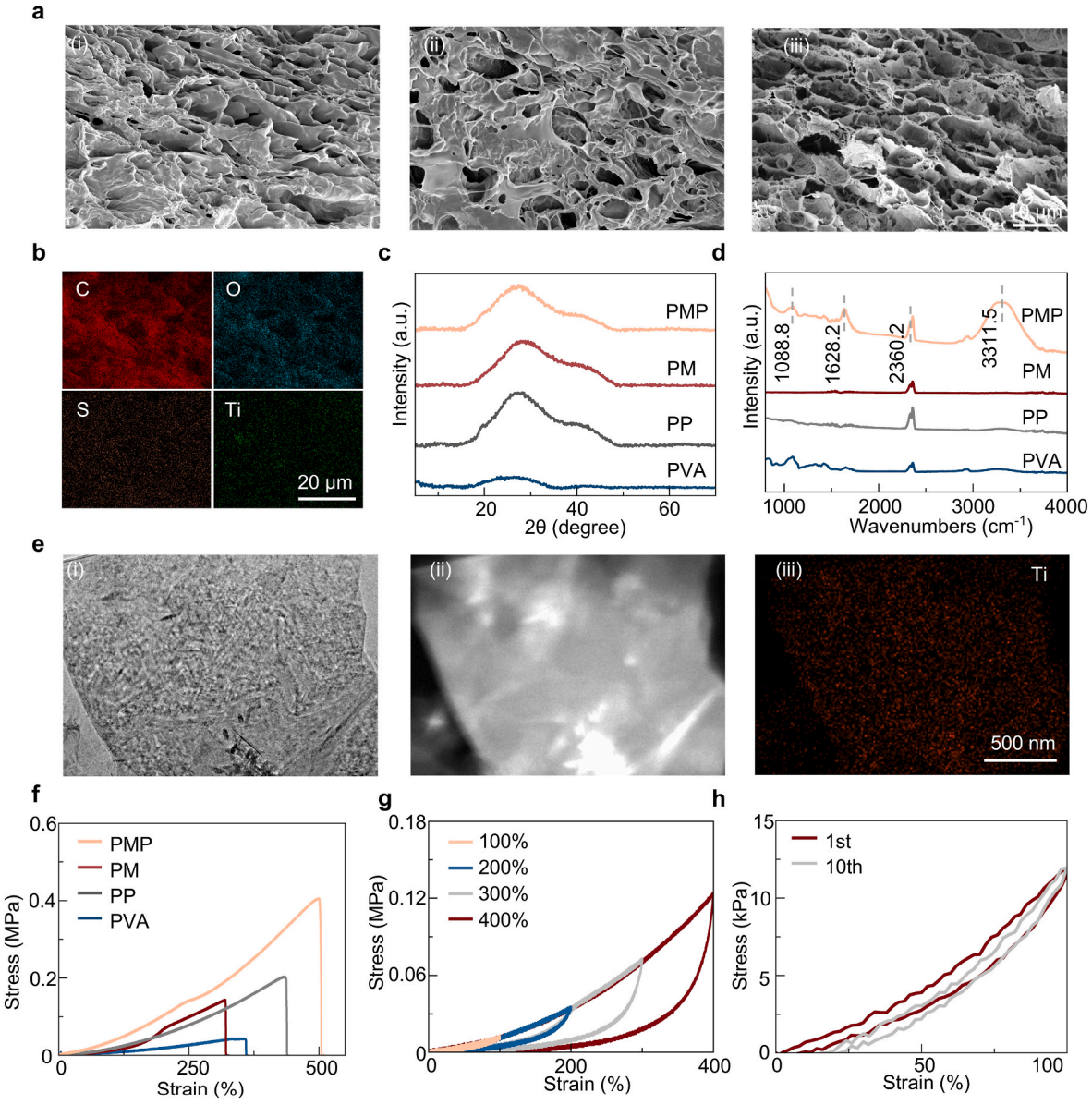

Fig. 2. Micro morphology and mechanical test of PMP hydrogel. **a**. (i) PM hydrogel SEM image. (ii) PP hydrogel SEM image. (iii) PMP hydrogel SEM image. **b**. PMP hydrogel EDS image. **c**. PMP hydrogel XRD curve. **d**. PMP hydrogel FTIR curve. **e**. (i) MXene SEM image. (ii) MXene TEM image. (iii) MXene EDS image. **f**. Stress-strain curves of hydrogels with different components. **g**. Stress-strain curve of PMP hydrogel with different tensile strengths. **h**. Stress-strain curves of the first and tenth PMP hydrogel.

intensity ultrasonic oscillation to uniformly disperse the polymer chains and conductive nanofillers at the molecular level. This ultrasonic solution generates a tightly cross-linked network with enhanced mechanical integrity and permeable conductive paths, reducing its resistivity and thereby providing a robust and efficient hydrogel matrix. Finally, it was repeatedly frozen and thawed three times to obtain the prepared hydrogel. In order to systematically analyze the relative contribution of each component to the overall performance, we used the same process to prepare four kinds of hydrogel, namely PVA, PVA MXene (PM), PVA PEDOT: PSS (PP), and PMP.

To explore the microscopic morphology, bonding, and hydrogelation of hydrogels, a series of physical image characterizations was carried out. In Fig. 2a, the scanning electron microscope (SEM) image shows that the PM hydrogel has a loose multilayer structure, while the cross-section of the PP hydrogel is a multi-microporous structure. After multiple freeze-thaw cycles, the PMP hydrogel still retains the typical layered wrinkled structure of MXene, with the PEDOT: PSS fiber networks interwoven to form a continuous porous skeleton. The synergy of layers and pores has constructed a loosely stratified three-dimensional structure, which is conducive to ion migration. Through Energy Dispersive Spectroscopy (EDS), we can observe that the Ti element in MXene and the S element in PEDOT: PSS are uniformly distributed in PMP hydrogel (Fig. 2b). And X-ray diffraction analysis (XRD) does not show obvious characteristic peaks, confirming the uniformity of the prepared hydrogel (Fig. 2c). In addition, to further illustrate the intermolecular interactions in PMP hydrogels, Fourier Transform infrared spectroscopy (FTIR) is used for analysis (Fig. 2d). The broad and strong absorption band at PMP hydrogel around 3311.5 cm^{-1} mainly results from the stretching vibration of PVA hydroxyl groups. Its peak shifts significantly toward higher wave numbers compared to pure PVA, indicating a notable change in the hydrogen bonding environment of PVA chains. This phenomenon is attributed to the dense and restricted hydrogen bonding network formed by the joint participation of the –OH/-F group on the MXene surface and the $–SO^{3-}$ group of PEDOT: PSS. The new peak at 1628.2 cm^{-1} is probably due to the bending vibration of physically adsorbed water or structure –OH on the surface of MXene, which confirms that $Ti_3C_2T_x$ nanoflakes have been successfully introduced into the hydrogel network, and there is a strong interface interaction between them and the polymer matrix. However, the weak signals near 2360 cm^{-1} in different component water hydrogel can be attributed to the interference absorption of atmospheric CO_2 in the test environment, which is independent of the material structure. Overall, FTIR spectroscopy analysis confirmed the formation of a tight composite network between PVA, MXene, and PEDOT: PSS through multiple hydrogen bonding interactions. These molecular-level bonds not only promote the uniform dispersion of conductive components but also improve mechanical strength and conductivity by restricting the movement of chain segments and optimizing the overlap of electron clouds. The microstructure characterization shows that PMP hydrogel has a layer pore double continuous structure, and tens to hundreds of nanometers of through-hole channels are orderly separated by MXene-rich nano sheet walls, forming a three-dimensional conductive network. This provides direct morphological evidence that PVA chains, MXene nanosheets, and PEDOT: PSS domains are assembled synergistically: PVA provides an elastic skeleton, MXene provides planar reinforcement and additional physical crosslinking points through hydrogen bonding and ion interactions, while PEDOT: PSS penetrates into interlayer channels to establish electronic pathways. The synergistic assembly of these three components improves the effective crosslinking density and limits chain slip, so that the hydrogel has higher mechanical integrity without sacrificing ductility. All phase analyses have verified the success and uniformity of PMP hydrogel preparation, and provided support for its subsequent good electrical conductivity and mechanical properties.

The good microstructure has laid the foundation for the excellent mechanical properties of the hydrogel [38,39]. High ductility and fatigue resistance jointly ensure that the electrode will not experience conductive path breakage or interface delamination during joint flexion and extension, cardiac pulsation, or respiratory fluctuations, avoiding signal drift and impedance increase, and ensuring continuous high-fidelity recording of microvolt-level neural potentials [40]. In addition, through the energy dissipation mechanism of dynamic covalent bond or physical interaction, the hydrogel can quickly restore its original shape and conductivity after repeated stretching.

To assess the mechanical properties of PMP hydrogel, the uniaxial tensile test (Fig. 2f) demonstrates that the hydrogel can be stretched to 500% of the engineering strain at a constant rate without fracturing. This provides direct mechanical evidence for the elongation of the PVA segment, the sliding of the MXene sheets, and the energy dissipation associated with the rigid microregions of PEDOT: PSS. The stress-strain curves of different tensile strengths show a monotonic upward trend without sudden stress drop or necking, indicating that the load is dispersed and dissipated through multi-scale mechanisms such as hydrogen bonding reconstruction and lamination (Fig. 2g). The Young's modulus of the linear region is 74 kPa (Figure S4 f), which overlaps with the skin microenvironment (20-200 kPa) and myocardial microenvironment (~100 kPa), significantly reducing interfacial shear forces and causing damage. Cyclic loading (0-100%, 10 cycles, Fig. 2h) shows that the curves of the first and tenth cycles almost overlap, indicating that the network has rapid elastic recovery and good fatigue resistance, meeting the dynamic requirements for long-term implantation. At the same time, as the next generation of bioelectronic interface materials, it also needs to have a certain degree of adhesion ability. As shown in Fig. 1d, hydrogels can immediately adhere to substrates such as plastics, magnets, wood, and silica hydrogel without additional glue, providing a universal interface solution for skin, implantable, and flexible packaging. In summary, the existence of the PMP network structure has improved its mechanical properties and adhesion ability, laying the foundation for its application as a biological interface electrode.

2.2. The electrical properties of PMP hydrogel

Mainstream conductive hydrogels often use physical intercalation by incorporating rigid conductive fillers like carbon nanotubes, graphene, or MXene into hydrophilic polymer matrices to enhance ion migration and electron transport [41]. This study reverts to the classic matrix-filled model, selects resilient PVA as the three-dimensional flexible scaffold, and utilizes its freeze-thaw crystal domain as the reversible physical crosslinking point to provide an energy dissipation mechanism. Meanwhile, MXene nanosheets are introduced as conductive additives. To resolve the contradiction between agglomeration and toughening, PEDOT: PSS is introduced to collaboratively construct a dual continuous conductive network. The abundant negatively charged terminals on the surface of MXene generate electrostatic attraction with the sulfonic acid groups on the PEDOT:PSS chain, thereby uniformly anchoring the MXene sheet within the conductive polymer framework and effectively reducing the defect density caused by agglomeration (Fig. 3a). At the same time, it can be clearly observed from Fig. 3a that the conductive mechanism of the conductive hydrogel is different from that of the metal electrode, that is, the conductive hydrogel is an ion electron cooperative transport, while the metal electrode only relies on free electrons. Moreover, the high specific surface area and metallic conductivity of MXene provide a fast electron pathway for PEDOT: PSS, while the ion conduction domain of PEDOT: PSS acts as an ion buffer pool. The two work together to achieve ion-electron dual-carrier transport, thereby obtaining high electrical conductivity while maintaining tensile toughness at a filler content lower than the traditional threshold.

To systematically analyze the relative contributions of each component to the overall conductive behavior, we successively prepared four hydrogels, namely PVA, PM, PP, and PMP, using the same process, and conducted parallel electrochemical tests under the same geometric area and moisture content conditions. The optimal formula was determined

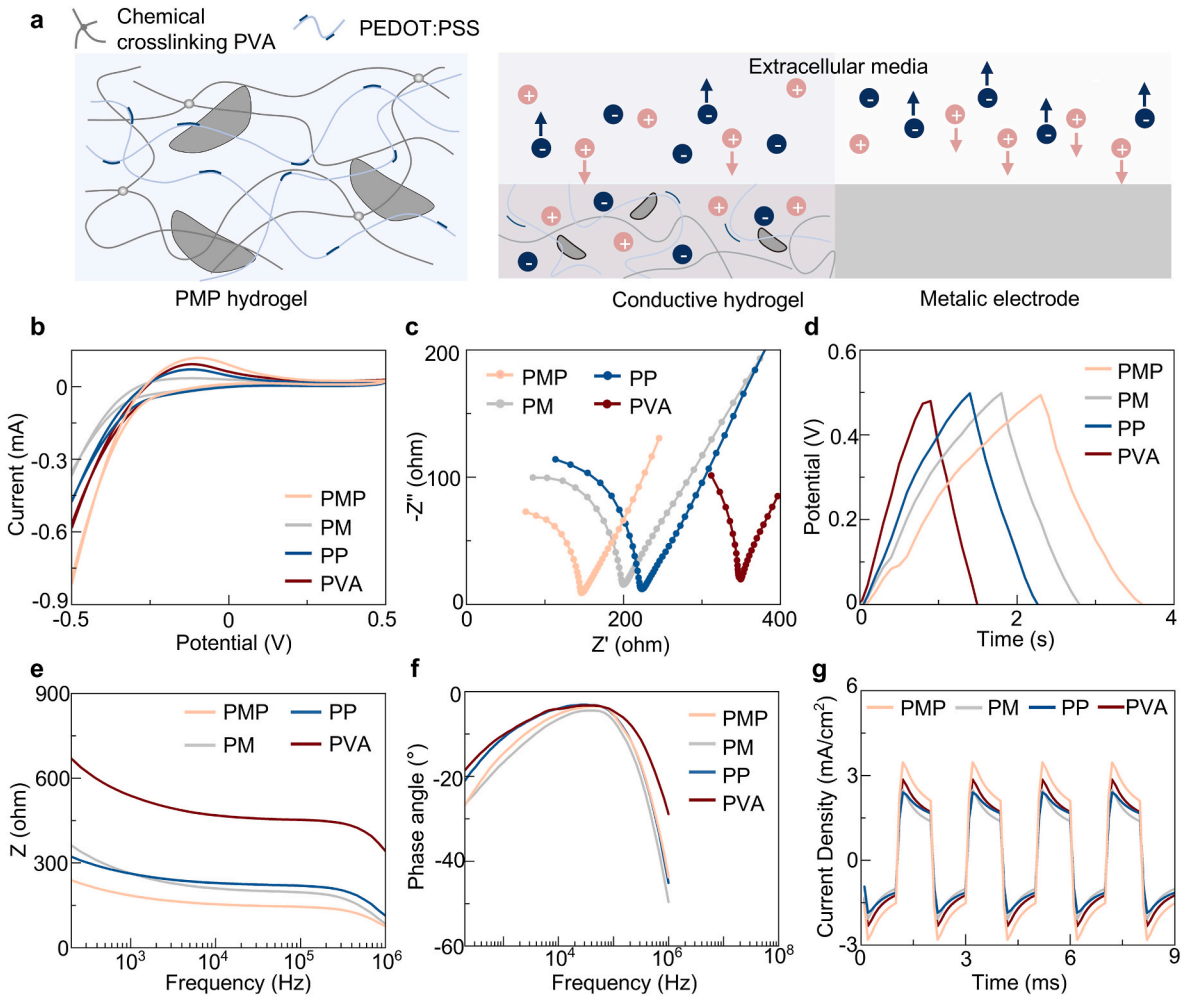

Fig. 3. PMP hydrogel conduction mechanism and electrical test. **a**. Schematic diagram of the PMP hydrogel mechanism. **b**. PMP hydrogel CV curve. **c**. PMP hydrogel EIS curve. **d**. PMP hydrogel GCD curve. **e**. PMP hydrogel Bode curve. **f**. PMP hydrogel Bode-Phase curve. **g**. PMP hydrogel I-T curve.

by fixing the total doping volume and systematically adjusting the volume ratio of MXene to PEDOT: PSS. The cyclic voltammetry (CV) results (Fig. 3b) show that the REDOX capacitance peak and integrated charge of the PMP hydrogel are significantly higher than those of any single-component hydrogel, indicating that the MXene-PEDOT: PSS dual network forms a continuous and reversible Faraday charge transfer path at the interface. Constant current charge-discharge (GCD, Fig. 3d) further confirms this feature. The discharge time of PMP is longer, indicating that the decrease in bulk resistance and the increase in the capacitance of the interface double layer work in synergy. In electrochemical impedance spectroscopy (EIS), the Nyquist plot (Fig. 3c) demonstrates that the volume conductivity of PMP is 0.913 mS cm^{-1}, surpassing that of the other three components. This observation confirms that the MXene-PEDOT: PSS dual network effectively contributes to the establishment of an efficient dual continuous pathway for electrons and ions through significant synergistic effects. The Bode phase diagram (Fig. 3e and f) shows that the impedance mode Z of PMP is lower than the other three, which is conducive to the distortion-free transmission of broadband physiological signals. In Fig. 3g, the potentiostatic ampere test further demonstrated that the charge injection capacity of PMP is stronger than that of any single-component combination. Meanwhile, the conductivity of the PMP hydrogel was confirmed through lighting experiments (Fig. S3). Besides, the video shows that there is a significant hysteresis effect after instantaneous lighting and extinguishing, confirming the existence of the ion-electron dual conductive network of the PMP hydrogel. By integrating CV, GCD, EIS, and amperometric data, when PMP hydrogels are combined, the system achieves the optimal electrical performance: high surface capacitance, low bulk resistance, and wideband independent conductivity occur simultaneously, providing a solid electrochemical foundation for the subsequent high-fidelity recording and efficient charge injection of bioelectronic interfaces. Meanwhile, Figure S4 a-c indicate that the electrical performance is better when the total volume of doped MXene and PEDOT: PSS is 1 mL and the volume ratio is 1:2. Overall, these electrochemical tests confirmed the superior interfacial conductivity of the PMP hydrogel, providing a solid electrical foundation for its dual-mode operation as a high-fidelity recording and efficient charge injection layer in the next-generation bioelectronic interface.

2.3. *The application of PMP hydrogel in bioelectronic interfaces*

To drive breakthroughs in neuroscience, precision medicine, and human-machine collaboration, the precise recording and stimulation of bioelectronic interfaces have become indispensable core technologies [42]. It is crucial to establish low resistance, bidirectional, and high fidelity energy and information channels between ion electron carriers to capture neural field potentials in real-time and achieve directional electrical stimulation, while preventing irreversible electrochemical reactions that may damage tissues. Table S1 shows that the PMP hydrogel in this study basically meets the above requirements in consideration of conductivity, mechanical strength, biosafety and hydrogel composition. To further validate the system, we conducted

bidirectional electrophysiological tests on SD rat neuromuscular model. On the other hand, non-invasive ECG and EMG monitoring was carried out in the forearms of volunteers to investigate their electrical and mechanical performance in the actual biological interface. This cross-species and cross-scale verification strategy provides direct experimental evidence for the transformation of PMP hydrogels into the fields of chronic implantation and wearable bioelectronics.

To evaluate the performance of PMP hydrogel as a bidirectional bioelectronic interface, we conducted a series of acute in vitro stimulation and recording experiments on the dissected sciatic nerve and gastrocnemius muscle of adult male rats. During the stimulation test phase (Fig. 4a–c), the same stimulation signal is provided through the PMP hydrogel membrane and commercial cuff electrodes, which are placed at the same position on the sciatic nerve. Although the peak amplitude of the PMP electrode was reduced compared with the cuff electrode, the latency and half-width were statistically the same, confirming the retention of time fidelity. During the recording and testing phase, the nerves are laterally cut to eliminate the outgoing feedback. Position the bipolar PMP electrode and the cuff electrode side by side around the sciatic nerve. Using the same stimulation signal, the PMP electrode was utilized as the stimulation electrode, while the cuff electrode served as the recording electrode. The recorded signals were then compared. Meanwhile, the signals collected by the sheet-like PMP electrode and the traditional needle-like electrode on the gastrocnemius muscle were compared. As can be observed from Fig. 4d–f, although the signal recorded by the PMP hydrogel still has the problem of a smaller amplitude compared with commercial cuff electrodes, the frequency and signal characteristics are basically retained, and effective stimulation signals can be recorded, which confirms the ability of the PMP hydrogel to collect signals as a biological click interface. Meanwhile, we placed the PMP hydrogel electrode on the gastrocnemius muscle and compared it with commercially available needle-shaped electrodes to collect signals from the muscle, further demonstrating the high efficiency and high fidelity of the PMP hydrogel as a recording electrode (Fig. 4g–i). In addition, the results of hematoxylin-eosin (HE) staining and blood biochemistry tests (Fig. S6) demonstrate that no abnormalities were observed after the PMP gel was implanted into the body for 4 weeks, indicating its good biocompatibility. Meanwhile, to demonstrate its safety in vivo, we conducted validation on L929 cells. In Fig. S5, cell viability staining and cck8 demonstrated that the PMP hydrogel has good biological safety. These results indicate that PMP hydrogels can simultaneously provide effective stimulation and high-fidelity neural recording in acute peripheral nerve models.

To assess the translational potential of PMP hydrogels as skin-compatible bioelectronic interfaces, we conducted non-invasive electrocardiogram (ECG) and electromyography (EMG) records on healthy human volunteers (Fig. 5a). During the ECG assessment, the subjects sat steadily. Replace the hydrogel material used in commercial Ag/AgCl electrodes with PMP and compare the recorded signals. The signals of the two groups of records are shown in Fig. 5b. It can be observed that the noise of the PMP hydrogel is relatively low. In terms of EMG, PMP, and commercial hydrogels were tested in a random order, with a 10-min break to avoid fatigue. Contract the right upper arm evenly and record its electromyographic signal. The characteristics of the two groups of signals (Fig. 5c) are roughly the same. In addition, we conducted long-term ECG monitoring on the same subject at different times, as shown in Fig. 5d. The difference in amplitude between the later test results and the first test is that the PMP hydrogel just prepared contains some groups

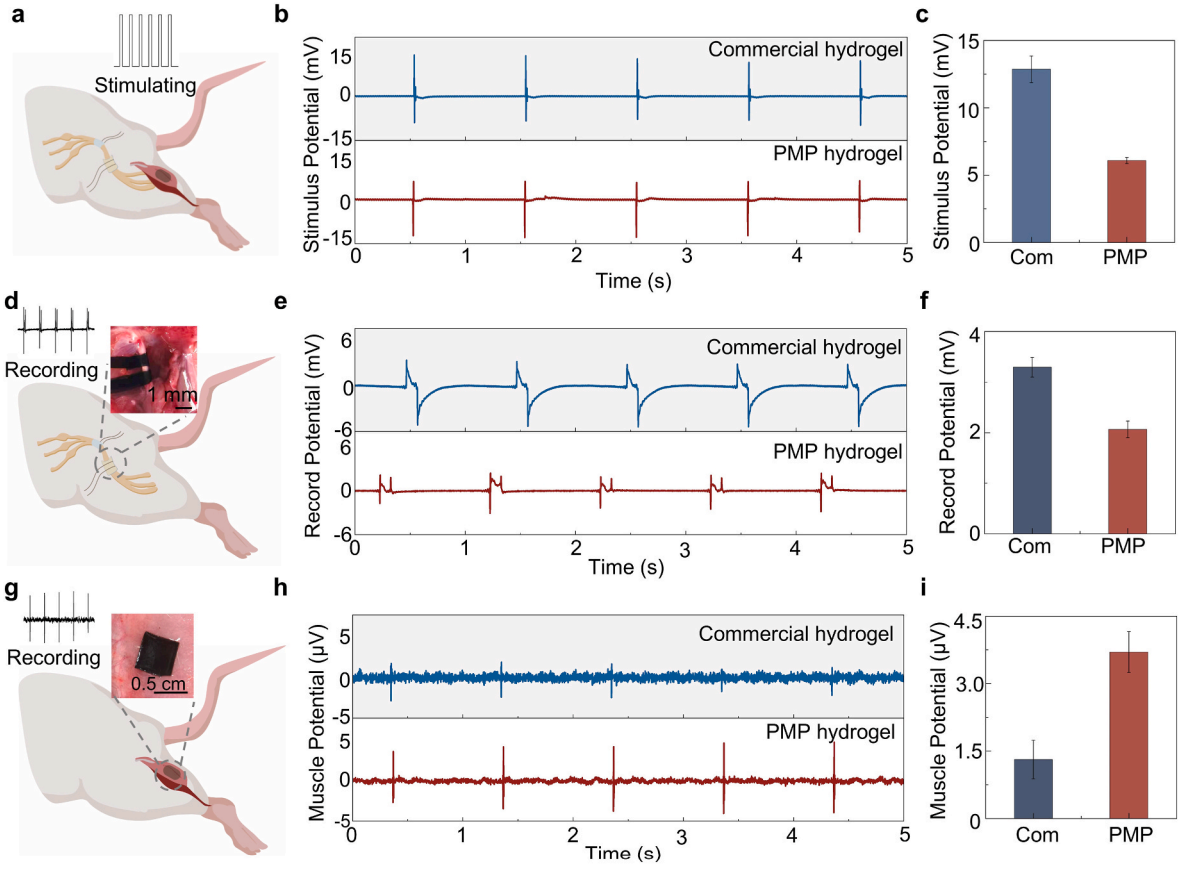

Fig. 4. Stimulation and recording of PMP hydrogel in rat leg nerves. **a**. Schematic diagram of PMP hydrogel sciatic nerve stimulation. **b**. PMP hydrogel sciatic nerve stimulation signal. **c**. PMP hydrogel sciatic nerve stimulation signal peak. **d**. Schematic diagram of PMP hydrogel sciatic nerve signal recording. **e**. PMP hydrogel sciatic nerve signal recording. **f**. PMP hydrogel sciatic nerve signal recording peak. **g**. PMP hydrogel gastrocnemius signal recording diagram. **h**. PMP hydrogel gastrocnemius signal recording. **i**. PMP hydrogel gastrocnemius signal recording peak.

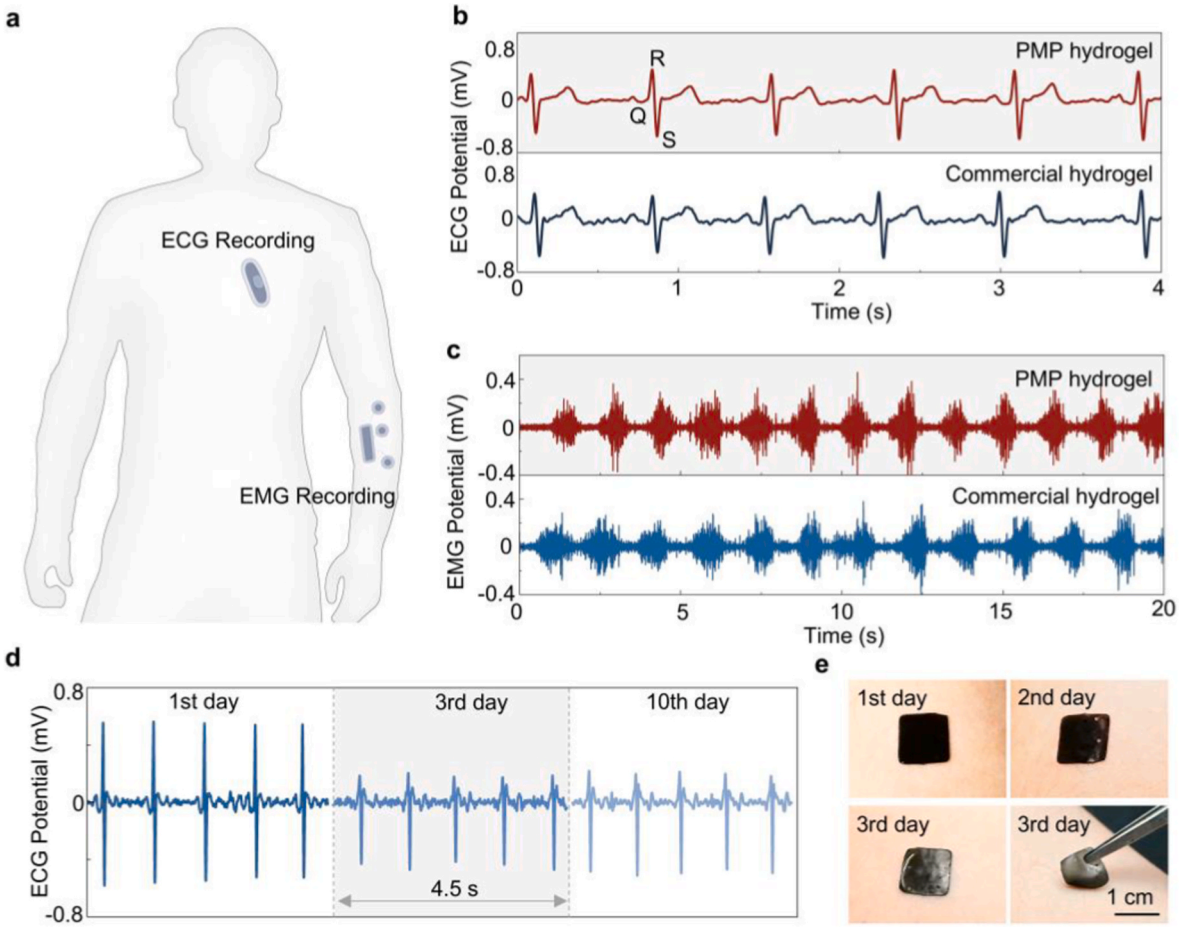

Fig. 5. Signal recording of PMP hydrogel on human body surface. **a**. Schematic diagram of human application of PMP hydrogel electrode. **b**. PMP hydrogel and commercial electrode ECG signal. **c**. PMP hydrogel and commercial electrode electromyography signal. **d**. ECG on the first, third and tenth days of PMP hydrogel. **e**. PMP electrode skin sensitivity test lasting for three days.

that are not oxidized. After sustained stability, it showed good signal stability and long-term persistence. And by monitoring the skin worn by the subjects for three days in Fig. 5e, it can be seen that the PMP hydrogel electrode has a low skin sensitivity. These results indicate that in conventional surface electrocardiogram and electromyogram recordings, PMP hydrogels have lower baseline noise and higher signal fidelity than standard conductive hydrogels, and have good biosafety.

Overall, our research results indicate that PMP hydrogels possess high mechanical modulus, adhesion, and electrical conductivity, which support their application in epidermal and neuromuscular biological interfaces. Excellent mechanical elasticity and adhesion ensure stable contact with biological tissues, while its high electrical conductivity guarantees accurate and reliable signal transmission. These observed characteristics highlight the potential of PMP hydrogels as candidates for the next generation of bioelectronic interfaces, which feature mechanical robustness, self-adhesion, and electrical reliability.

3. Conclusion

In conclusion, this study proposed a strategy to build a robust hydrogel with ion electron double conductivity enhancement network, which achieved a balanced combination of conductivity, ductility and biocompatibility. Additionally, the electrostatic interaction between the surface functional groups of MXene and PEDOT chains facilitates the uniform dispersion of rigid nanofillers, while MXene contributes to the ion-electron dual conductive network of PEDOT: PSS. Therefore, a conductivity of 0.913 mS cm^{-1} was obtained. This network is supported by PVA as the supporting framework, and PEDOT: PSS and MXene form hydrogen bonds with PVA through surface groups. Endow the hydrogel with high tensile strength (>500%) and high toughness (74 kPa). These synergistic properties make it possible to achieve stable and high-fidelity electrophysiological signals in both animals and humans, as reliable electrocardiogram and electromyogram records have shown. Overall, this study not only addresses the ongoing challenges in the development of conductive polymer hydrogels but also offers a promising approach to promoting the application of the next generation of hydrogel-based bioelectronic interfaces.

4. Experimental methods

4.1. Materials

Ti_3AlC_2 powder was purchased from 11 Technology. PVA (1799) and lithium fluoride (LiF, AR) were purchased from Aladdin. Concentrated hydrochloric acid (HCl, 36.5%) was purchased from Macklin. PEDOT: PSS solution was bought from Aladdin. Cuff electrode solution was bought from Kedou BC.

4.2. Materials synthesis and preparation

The MXene solution was prepared using the following method. First, etching: 5 mL of deionized (DI) water was added to 15 mL of 36%–38% HCl to prepare solution A. Then, 1 g of LiF and 1 g of MAX phase (Ti_3AlC_2) were dissolved in solution A to obtain the MXene solution, which was stirred at 40 °C for 24 h. The PVA solution was prepared as follows. 1.3 g of PVA powder was mixed with 8.7 g of DI water at 98 °C

for 2 h to get the PVA solution.

The prepared MXene solution and the purchased PEDOT: PSS solution was mixed into the prepared PVA solution and stirred at room temperature for 2 h to obtain the PMP hydrogel precursor. Then, it was placed under high-intensity ultrasonic oscillation for 5 min to obtain a uniformly dispersed PMP hydrogel precursor. Finally, pour the well-dispersed PMP hydrogel precursor into a 2.5 cm*2.5 cm mold prepared in advance, and then place it in the freezer compartment of the refrigerator for 12 h, repeatedly freezing and thawing three times to obtain the formed PMP hydrogel.

4.3. Characterization measurements

The cross-section and related elemental information of the PMP hydrogel were characterized using scanning electron microscopy (SEM) and energy-dispersive spectroscopy (EDS) with the NOVA450 instrument. The chemical composition and state of the PMP hydrogel sample were analyzed via X-ray photoelectron spectroscopy (XPS). Additionally, the crystal structure and fundamental composition were examined through X-ray diffractometry (XRD) with a PANalytical X'Pert3 system, utilizing Cu Kα radiation ($\lambda = 1.5406$ Å) at settings of 40 kV and 40 mA over a 2θ range of 5° to 10°. The tensile properties of the hydrogel were assessed at room temperature using the ESM301/Mark-10 testing system.

4.4. Electrochemical measurements

Cut the PMP hydrogel into rectangles of 1 *1.5 cm to ensure that its size in the PBS solution is 1*1 cm after being clamped by the fixture. A three-electrode system was established using PMP hydrogel electrodes, platinum sheet electrodes, and calomel electrodes for testing. CV, GCD, EIS, and CA tests were conducted using an electrochemical workstation (CHI660E).

The conductivity is calculated based on the Nyquist curve obtained from the EIS test.

$$k = L \div (Z \times A)$$

Here, k denotes electrical conductivity, L refers to the material's thickness, A represents the material's surface area, and Z indicates the intersection point value of the Nyquist curve with the horizontal axis.

4.5. Animal nerve stimulation and recording

We took adult male SD rats and felt the position of the femur on the thigh with our fingers. Using this as a bony marker, we cut the skin in the superficial layer of the femur, and the incision was made at the projection position of the femur on the body surface. After opening the skin, a distinct white line can be seen, which is the fascia between the muscles. A small cut is made along this white line, and a vascular forceps is inserted to separate it bluntly along the direction of the white line. After separating the white line, the sciatic nerve trunk between the two muscles can be seen. A slight downward separation reveals the separated tibial nerve and the common peroneal nerve. Cut the PMP hydrogel into long strips of 1 mm*25 mm and encapsulate them in parallel in a film. At the same time, cut out a 5 mm*25 mm electrode patch for subsequent muscle signal recording. Then, the encapsulated electrode was placed parallel to the commercial cuff electrode on the dissected sciatic nerve. When the cuff electrode is used as the stimulation electrode, the PMP electrode is used as the recording electrode to record the signal. When using the PMP electrode as the stimulation electrode, the cuff electrode is used as the recording electrode to record the signal. At the same time, the leg muscles are separated, and the PMP electrode patch is used to record the signal and compare it with the signal recorded by the needle electrode, thereby directly evaluating the signal fidelity and interface impedance characteristics. The stimulation signal uses square wave pulses with a frequency of 1 Hz, an amplitude of 100 μA, and a pulse width of 100 ms. The stimulation device uses an electrophysiological signal recording system, and the recording device uses an MP150 electromyography recording module. All rat experiments were performed according to protocols approved by the Committee on Ethicsof the Beijing Institute of Nanoenergy and Nanosystems (2025041LZ).

4.6. Human electrocardiogram and electromyogram records

The PMP hydrogel was cut into circles with a diameter of 1 cm to replace the hydrogel material on commercial Ag/AgCl electrodes. When the subjects were in a stable sitting position, commercial hydrogel electrodes were used to record electrocardiogram signals, respectively, with the PMP hydrogel electrodes we prepared for comparison. Then, when the subject was sitting steadily, fixed electrodes at intervals of 4 cm on the subject's right upper arm, and then let the subject's right arm exert force steadily to record the electromyographic signals. In addition, it should be pasted at a fixed position for long-term stability tests, and records should be made on the 1st, 3rd, and 10th days, respectively. At the same time, it should be pasted on a stable part of the forearm for skin sensitivity tests, and photos should be taken at the above-mentioned times for the record. The physiological signals of the human body are recorded by using the recording equipment mentioned above.

4.7. Cell biocompatibility and proliferation evaluations

L929 cell was cultured in Dulbecco's Modified Eagle Medium (DMEM, Gibco), enriched with 10% fetal bovine serum and 1% penicillin-streptomycin. Cells were grown at 37 °C, in humidified air containing 5% CO_2. To assess cytocompatibility, 10 mg of each material was immersed in 20 mL of DMEM and incubated at 4 °C for 72 h to prepare the sample leachate.

L929 cells were cultured in these extracts for 48 h, and absorbance at 450 nm was measured using a microplate reader (Thermo Fisher Scientific) after incubation with CCK-8. Cytotoxicity was further assessed by live/dead cell imaging. L929 cells were co-stained with Calcein-AM and PI and imaged using an inverted fluorescence microscope.

4.8. Biological safety verification

To verify the biocompatibility of the implanted electrodes, we subcutaneously implanted the electrodes and established a control group, which only had a wound made at the same location without implantation. Four weeks after implantation, hematoxylin and eosin (HE) staining was performed on the heart, liver, spleen, lungs, and kidney of both groups. Whole blood samples were placed at room temperature for 2 h, and then centrifuged at 3000 rpm for 15 min at 2-8 °C. The supernatant was collected for blood biochemical tests, including alkaline phosphatase (ALP), blood urea nitrogen (BUN), and creatinine (CR).

CRediT authorship contribution statement

Yumeng Zhang: Data curation, Formal analysis, Visualization, Writing – original draft. **Chang Zhu:** Investigation, Visualization. **Han Ouyang:** Funding acquisition. **Xiangxiang Wang:** Visualization. **Jian Cheng:** Visualization. **Xiong Pu:** Visualization. **Engui Wang:** Funding acquisition, Supervision, Visualization, Writing – review & editing. **Zhou Li:** Conceptualization, Data curation, Funding acquisition, Project administration, Supervision, Writing – review & editing.

Declaration of competing interest

The authors declare that they have no known competing financial interests or personal relationships that could have appeared to influence the work reported in this paper.

Acknowledgements

This work was supported by the National Natural Science Foundation of China grants 52373256 (to H.O.), T2125003 (to Z.L.), U25A20417 (to Z.L.); Beijing Natural Science Foundation grants 7232347 (to H.O.), 7264408 (to E.W.), L245015 (to Z.L.), Z240022 (to Z.L.)and 25JL006 (to Z.L.); Youth Innovation Promotion Association CAS grant 2023176 (to H.O.); Beijing Nova Program grant 2024047 (to H.O.); Fundamental Research Funds for the Central University grant.

Appendix A. Supplementary data

Supplementary data to this article can be found online at https://doi.org/10.1016/j.mtchem.2026.103832.

Data availability

Data will be made available on request.

References

[1] R. Hu, B. Yao, Y. Geng, S. Zhou, M. Li, W. Zhong, F. Sun, H. Zhao, J. Wang, J. Ge, R. Wei, T. Liu, J. Jin, J. Xu, J. Fu, High-fidelity bioelectrodes with bidirectional ion–electron transduction capability by integrating multiple charge-transfer processes, Adv. Mater. 36 (2024) 2403111, https://doi.org/10.1002/adma.202403111.

[2] J. Shen, S. Wu, Y. Wang, Z. Yan, T. Liu, X. Sun, Y. Qian, Mechano-bioactive hydrogel bioelectronics for mechanical-electrical-bioenergetic conversion and glia-modulating neural regeneration, Nat. Commun. 16 (2025) 11582, https://doi.org/10.1038/s41467-025-66779-5.

[3] Y. Lu, Z. Jin, Y. Jian, D. Kong, H. Zhou, Y. Xu, R. Cao, Z. Xia, F. Yang, Q. Wu, Y. Gao, A. Cui, S. Yang, N. Zheng, J. Bang, G. Yang, S.H. Ko, H. Yang, K. Xu, Metal–hydrogel chelation interfaces for ultrasoft and bidirectional bioelectronics, Natl. Sci. Rev. 12 (2025), https://doi.org/10.1093/nsr/nwaf399.

[4] X. Huang, N. Yang, S. Sun, Y. Cheng, L. Cheng, Recent progress of hydrogel-based bioelectronics for mechanophysiological signal sensing, Mater. Sci. Eng. R Rep. 162 (2025) 100888, https://doi.org/10.1016/j.mser.2024.100888.

[5] A. Wahlsten, A. Stracuzzi, I. Lüchtefeld, G. Restivo, N. Lindenblatt, C. Giampietro, A.E. Ehret, E. Mazza, Multiscale mechanical analysis of the elastic modulus of skin, Acta Biomater. 170 (2023) 155–168, https://doi.org/10.1016/j.actbio.2023.08.030.

[6] C.F. Guimarães, L. Gasperini, A.P. Marques, R.L. Reis, The stiffness of living tissues and its implications for tissue engineering, Nat. Rev. Mater. 5 (2020) 351–370, https://doi.org/10.1038/s41578-019-0169-1.

[7] S.J. Mostafavi Yazdi, J. Baqersad, Mechanical modeling and characterization of human skin: a review, J. Biomech. 130 (2022) 110864, https://doi.org/10.1016/j.jbiomech.2021.110864.

[8] L. Shan, Y. Xue, X. Chen, Y. Wang, Y. Feng, L. Dong, C. Wang, P. Zhang, F. Wang, L. Guo, J. Liu, Mechanically compliant and impedance matching hydrogel bioelectronics for low-voltage peripheral neuromodulation, Adv. Mater. 38 (2026) e11014, https://doi.org/10.1002/adma.202511014.

[9] H. Cao, L. Duan, Y. Zhang, J. Cao, K. Zhang, Current hydrogel advances in physicochemical and biological response-driven biomedical application diversity, Signal Transduct. Targeted Ther. 6 (2021) 426, https://doi.org/10.1038/s41392-021-00830-x.

[10] S.B. Hong, J.-O. Jeong, H. Choi, Hydrogels in cardiac surgery: versatile platforms for tissue repair, adhesion prevention, and localized therapeutics, Gels 11 (2025) 564.

[11] S. Almawash, S.K. Osman, G. Mustafa, M.A. El Hamd, Current and future prospective of injectable hydrogels-design challenges and limitations, Pharmaceuticals 15 (2022), https://doi.org/10.3390/ph15030371.

[12] M. Sun, Q. Lu, Z.L. Wang, B. Huang, Understanding contact electrification at liquid–solid interfaces from surface electronic structure, Nat. Commun. 12 (2021) 1752, https://doi.org/10.1038/s41467-021-22005-6.

[13] G. Zhu, N. Javanmardia, L. Qian, F. Jin, T. Li, S. Zhang, Y. He, Y. Wang, X. Xu, T. Wang, Z.-Q. Feng, Advances of conductive hydrogel designed for flexible electronics: a review, Int. J. Biol. Macromol. 281 (2024) 136115, https://doi.org/10.1016/j.ijbiomac.2024.136115.

[14] J.H. Zhuang, Z. Li, Y. Liang, T. Tang, X.Y. Hu, R. Ou, Q.J. Ma, B.Y. Zhang, Y. F. Cheng, W.L. Feng, J.Z. Ou, Recent progress in two-dimensional materials: from emerging structures and synthesis approaches to electronic and sensing applications, Chem. Eng. J. 520 (2025) 166133, https://doi.org/10.1016/j.cej.2025.166133.

[15] O. Folorunso, P. Olukanmi, S. Thokozani, Conductive polymers' electronic structure modification for multifunctional applications, Mater. Today Commun. 35 (2023) 106308, https://doi.org/10.1016/j.mtcomm.2023.106308.

[16] J.N. Lemke, J. Fiocchi, C.A. Biffi, A. Tuissi, F. Copes, C. Paternoster, D. Mantovani, A. Coda, Design, development and performance of a Fe–Mn–Si–Cu alloy for bioabsorbable medical implants, J. Mater. Chem. B 13 (2025) 2737–2752, https://doi.org/10.1039/D4TB01635A.

[17] M. Zhang, S. Xu, R. Wang, Y. Che, C. Han, W. Feng, C. Wang, W. Zhao, Electrospun nanofiber/hydrogel composite materials and their tissue engineering applications, J. Mater. Sci. Technol. 162 (2023) 157–178, https://doi.org/10.1016/j.jmst.2023.04.015.

[18] C. Wang, Y. Liu, X. Qu, B. Shi, Q. Zheng, X. Lin, S. Chao, C. Wang, J. Zhou, Y. Sun, G. Mao, Z. Li, Ultra-stretchable and fast self-healing ionic hydrogel in cryogenic environments for artificial nerve fiber, Adv. Mater. 34 (2022) 2105416, https://doi.org/10.1002/adma.202105416.

[19] C. Zhang, Y. Zhang, Y. Wang, Y. Huang, Advances in conductive filler-integrated hydrogels and derived aerogels: innovative strategies for electromagnetic interference shielding, Mater. Horiz. 12 (2025) 7066–7100, https://doi.org/10.1039/D5MH00577A.

[20] B. Yao, Y. Yan, Q. Cui, S. Duan, C. Wang, Y. Du, Y. Zhao, D. Wu, S. Wu, X. Zhu, T. Hsiai, X. He, Ultrastrong, highly conductive and capacitive hydrogel electrode for electron-ion transduction, Matter 5 (2022) 4407–4424, https://doi.org/10.1016/j.matt.2022.09.004.

[21] Chen, X.;Wang, L.;Duan, Q.;Zheng, Z.;Xue, Y.;Feng, Y.;Lu, Y.; Liu, J. Integrated hydrogel optical fiber electronics with mechanically robust interfaces enable simultaneous electrophysiological recording and optogenetic modulation. Adv. Mater., *n/a*, e17771. https://doi.org/10.1002/adma.202517771.

[22] X. Li, J.P. Gong, Design principles for strong and tough hydrogels, Nat. Rev. Mater. 9 (2024) 380–398, https://doi.org/10.1038/s41578-024-00672-3.

[23] B.S. Kaith, A. Singh, A.K. Sharma, Sud, D. Hydrogels: synthesis, classification, properties and potential applications—A brief review, J. Polym. Environ. 29 (2021) 3827–3841, https://doi.org/10.1007/s10924-021-02184-5.

[24] R. Luo, Y. Xiong, J. Li, M. Xiao, Y. Bai, Z. Xu, Z. Luo, C. Li, A. Liang, H. Feng, Z. Li, Piezoelectric injectable anti-adhesive hydrogel to promote endogenous healing of tendon injuries, Adv. Mater. 37 (2025) 2501306, https://doi.org/10.1002/adma.202501306.

[25] M. Xiao, J. Meng, H. Zhang, Z. Wu, Z. Li, Ionic gels for low-grade heat energy harvesting and thermal sensing, Adv. Mater. 37 (2025) e06436, https://doi.org/10.1002/adma.202506436.

[26] Y. Quan, E. Wang, H. Ouyang, L. Xu, L. Jiang, L. Teng, J. Li, L. Luo, X. Wu, Z. Zeng, Z. Li, Q. Zheng, Biodegradable and implantable triboelectric nanogenerator improved by β-Lactoglobulin fibrils-assisted flexible PVA porous film, Adv. Sci. 12 (2025) 2409914, https://doi.org/10.1002/advs.202409914.

[27] Y. Wu, Y.X. Chen, J. Yan, D. Quinn, P. Dong, S.W. Sawyer, P. Soman, Fabrication of conductive gelatin methacrylate–polyaniline hydrogels, Acta Biomater. 33 (2016) 122–130, https://doi.org/10.1016/j.actbio.2016.01.036.

[28] X. Wan, M. Liu, F. Zhang, L.-P. Xu, S. Wang, Interfacial chemistry in functional hydrogel coatings, Angew. Chem. Int. Ed. 64 (2025) e202425552, https://doi.org/10.1002/anie.202425552.

[29] Y. Hou, S. Ma, J. Hao, C. Lin, J. Zhao, X. Sui, Construction and ion transport-related applications of the hydrogel-based membrane with 3D nanochannels, Polymers 14 (2022) 4037.

[30] X. Hu, L. Tan, X. Wu, J. Wang, Interlayer engineering in 3D graphene skeleton realizing tunable electronic properties at a highly controllable level for piezoresistive sensors, Nano Res. 16 (2023) 8512–8521, https://doi.org/10.1007/s12274-023-5710-2.

[31] J. Bai, S. Feng, Y.N. Ye, W. Yu, Q. Zheng, F. Zhu, Thermally programmable off-equilibrium pathways in salt-doped polyelectrolyte hydrogels, Macromolecules 58 (2025) 13144–13153, https://doi.org/10.1021/acs.macromol.5c02742.

[32] W. Li, Z. Chen, C. Xu, X. Zhao, C. Ren, P. Wei, D. Zhang, Y. Yin, F. Guan, W. Zhai, K. Dai, A seamlessly integrated sandwich-structured hydrogel for supercapacitors and multimodal wearable sensors enabling information transmission, Adv. Funct. Mater. 35 (2025) e12653, https://doi.org/10.1002/adfm.202512653.

[33] S. Yin, Y. Ding, Y. Zhang, C. Zhou, C. Qian, G. Che, C. Zhao, L. Jiang, Superstrong and transparent hydrogels with homogeneous multiple networks, Macromolecules 58 (2025) 4357–4364, https://doi.org/10.1021/acs.macromol.4c03202.

[34] H. Sun, S. Wang, P. Wang, L. Bai, M. Tan, F. Yang, R. Wang, X. He, Highly stretchable, adhesive, and conductive PEDOT nanocomposite hydrogels for high-performance flexible bioelectronics, Adv. Sci. 12 (2025) e13487, https://doi.org/10.1002/advs.202513487.

[35] D. Bao, X. Ji, F. Guan, J. Geng, Z. Li, Y. Xu, Q. Yang, Y. Shi, J. He, S. Zhang, J. Guo, Ordered nanostructures formed by multi-interactions for toughening the ultrastretchable conductive hydrogel, Macromolecules 58 (2025) 12353–12365, https://doi.org/10.1021/acs.macromol.5c01625.

[36] Y. Liu, J. Zhang, D. Wang, Preparation schemes and applications of multifunctional PVA composite hydrogels, Chem. Eng. J. 508 (2025) 160946, https://doi.org/10.1016/j.cej.2025.160946.

[37] A. Ullah, D.Y. Kim, S.I. Lim, H.-R. Lim, Hydrogel-based biointerfaces: recent advances, challenges, and future directions in human–machine integration, Gels 11 (2025) 232.

[38] X. Yan, H. Huang, A.M. Bakry, W. Wu, X. Liu, F. Liu, Advances in enhancing the mechanical properties of biopolymer hydrogels via multi-strategic approaches, Int. J. Biol. Macromol. 272 (2024) 132583, https://doi.org/10.1016/j.ijbiomac.2024.132583.

[39] J. Fu, M. in het Panhuis, Hydrogel properties and applications, J. Mater. Chem. B 7 (2019) 1523–1525, https://doi.org/10.1039/C9TB90023C.

[40] D. Zhong, Z. Wang, J. Xu, J. Liu, R. Xiao, S. Qu, W. Yang, A strategy for tough and fatigue-resistant hydrogels via loose cross-linking and dense dehydration-induced

entanglements, Nat. Commun. 15 (2024) 5896, https://doi.org/10.1038/s41467-024-50364-3.

[41] S. Zhang, B. Zhao, D. Zhang, M. Yang, X. Huang, L. Han, K. Chen, X. Li, R. Pang, Y. Shang, A. Cao, Conductive hydrogels incorporating carbon nanoparticles: a review of synthesis, performance and applications, Particuology 83 (2023) 212–231, https://doi.org/10.1016/j.partic.2023.06.002.

[42] P. Lu, D. Ruan, M. Huang, M. Tian, K. Zhu, Z. Gan, Z. Xiao, Harnessing the potential of hydrogels for advanced therapeutic applications: current achievements and future directions, Signal Transduct. Targeted Ther. 9 (2024) 166, https://doi.org/10.1038/s41392-024-01852-x.